Measurements of radiative-decay rates of the $2s^22p(^2P^\circ)$-$2s2p^2(^4P)$ intersystem transitions of C II

Z. Fang, Victor H. S. Kwong, and Jiebing Wang
Physics Department, University of Nevada–Las Vegas, Las Vegas, Nevada 89154

W. H. Parkinson
Harvard-Smithsonian Center for Astrophysics, 60 Garden Street, Cambridge, Massachusetts 01238
(Received 3 February 1993)

The radiative-decay rates of the $2s^22p(^2P^\circ)$-$2s2p^2(^4P)$ intersystem transitions of C^+ ions have been measured by recording the time dependence of the ~233-nm emission. A cylindrical radio-frequency ion trap was used to store electron-impact-produced C^+ ions. The time-dependent signals were analyzed by multiexponential least-squares fits to the data. The measured radiative-decay rates to the ground term are 146.4(+8.3,−9.2) s^{-1} for $^4P_{1/2}$, 11.6(+0.8,−1.7) s^{-1} for $^4P_{3/2}$, and 51.2(+2.6,−3.5) s^{-1} for $^4P_{5/2}$. Comparison of the measured values with theoretical values is presented.

PACS numbers: 32.70.Fw, 95.30.Dr, 32.80.Pj

I. INTRODUCTION

The boronlike ions of carbon, nitrogen, and oxygen are astrophysically abundant and their spectra are observed in a large number of astronomical sources. The atomic structure of the B-like ion leads to spin-changing, intersystem lines, emitted by the decay of the fine-structure levels of the $2s2p^2(^4P)$ metastable term to the ground term $2s^22p(^2P^\circ)$. Often, all five lines of the intercombination multiplet (UV 0.01) are measurable features in these sources. C II, N III, and O IV lines are observed, for example, in late-type giant stars [1–3], in the solar chromosphere [4], the solar transition region [5, 6] and in symbiotic stars [7, 8].

Because the rates for collisional excitation and deexcitation of ions in the diffuse atmospheres of these objects are comparable with the radiative-decay rates for intersystem and forbidden transitions, intensity ratios involving intersystem lines within the multiplet [9, 10], or with forbidden or allowed lines [11], can be applied to determine electron density and temperature. The line ratios depend critically on the decay rates, i.e., the transition probabilities (A values), and thus the accuracies of the density and temperature diagnostic techniques depend strongly on the completeness and accuracy of the A-value data for the transitions involved. Until now, the A values for the lines of multiplet (UV 0.01) of C II, N III, and O IV were known only by theoretical means [12–15] or, in the case of C II, also by empirical estimates [10]. The present paper reports the first measurements of the values of the radiative lifetimes for the $J = \frac{5}{2}$, $\frac{3}{2}$, and $\frac{1}{2}$ levels of the $2s2p^2(^4P)$ metastable term of C II. Similar measurements are underway on the N III multiplet.

II. EXPERIMENTAL METHODS

The $2s2p^2(^4P)$ term of C^+ ion has three fine-structure levels and all three levels, $^4P_{1/2}$, $^4P_{3/2}$, and $^4P_{5/2}$, decay by electric-dipole spin-changing transitions to the ground $2s^22p(^2P^\circ)$ term (Fig. 1). The emission consists of five closely spaced lines at 232.54 nm, 232.88 nm, 232.42 nm, 232.76 nm, and 232.61 nm [16]. The radiative lifetimes of the levels of the ^4P term were obtained by measuring the unresolved spontaneous emission from metastable C^+ ions stored in a cylindrical radio-frequency ion trap. Since the ion trap is a low-density source and the intersystem lines of this compact multiplet are intrinsically weak, it was not possible with this experimental arrangement to resolve spectroscopically the separate line components of the emission. The photon signal from the unresolved emission is expected to consist of three exponential decay components which correspond to the radiative decay

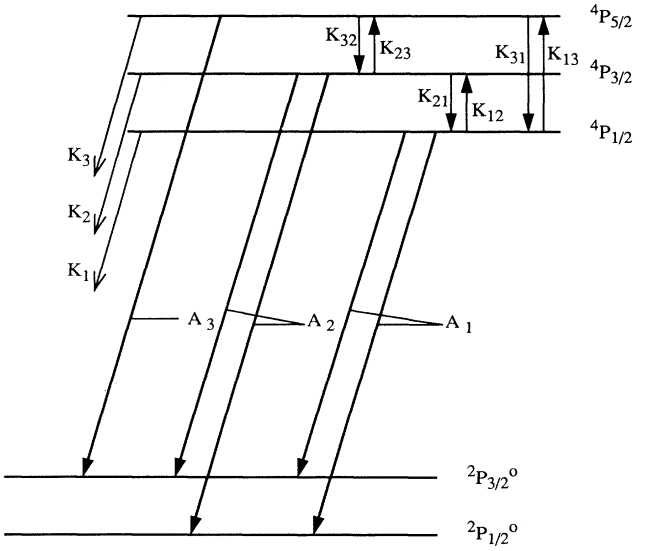

FIG. 1. Energy-level diagram for multiplet (UV 0.01) of C II, $2s^22p(^2P^\circ)$-$2s2p^2(^4P)$.

 ©1993 The American Physical Society

of the fine structure $^4P_{1/2}$, $^4P_{3/2}$, and $^4P_{5/2}$ levels of the ^4P term. A multiexponential function is used for the data analysis. Similar analysis has been used on the nearly analogous radiative decays in Si II [17] of the fine-structure levels of the $3s3p^2(^4P)$ metastable term to the ground term $3s^23p(^2P^\circ)$. We will discuss the analysis of multiexponential decay components in some detail in Sec. III A.

The apparatus and experimental method used in this experiment are the same as that used for the measurement of the A value of the $2s^2(^1S_0)$-$2s2p(^3P_1^\circ)$ intersystem line of C III [18]. The cylindrical ring electrode of the ion trap was constructed from 30-gauge, 304 stainless-steel mesh. A 2-cm-diam hole was cut from the mesh facing the optics and was covered by a finer mesh to permit 95% transmission of photons. The electrode of radius $r_0 = 1.67$ cm defined the radial extent of the trap, which was axially closed by two planar end caps separated by $2r_0$. With the end caps grounded and electrically insulated from the ring electrode, a time-varying voltage $V(t) = U_0 + V_0\cos(\Omega_0 t)$ applied to the ring electrode produced an effective potential well [19] that confined an ion population to a central region bounded by the electrodes. The measurements were carried out with $\Omega_0/2\pi = 1.2$ MHz, $V_0 = 400$ V, and $U_0 = 30$ V, yielding pseudopotential near-spherical well depths of $D_z = 15.8$ eV and $D_r = 19.0$ eV in the axial and radial directions, respectively. Test measurements were made with D_z potential-well depths ranging from 2.5 eV to 15.8 eV and no changes were observed in the radiative decay. No photon signal was observed when the ion trap was adjusted so that C^+ ions were excluded from the trap.

C^+ ions were produced and excited during a 5-ms period of electron bombardment of high-purity (99.97%) CO gas with an unfocused pulsed electron beam from a BaO dispenser cathode biased to -55 V. Immediately after the ions were created, the cathode was biased to $+125$ V. This bias inhibited the emission of electrons from the cathode and eliminated continuous ion production. After the production-excitation phase there was a 0.5-msec relaxation period, during which time all allowed transitions decayed. This is followed by a long 410-msec photon detection period.

Photons from the stored ions were collected by a fast, $f/1.4$ lens system, composed of two Suprasil lenses with a $\times 1.5$ magnification, spectrally filtered, and detected by a solar-blind photomultiplier (EMR 541Q-05M-13), operated in the pulse counting mode. The photon signal was binned and stored in an Ortec multichannel scalar (MCA) at 0.4 msec per channel.

A narrow-band interference filter (Acton Research Corp.) with central wavelength at 232 nm and bandwidth ± 10 nm was installed in the optical system to isolate the C II emission. The filter attenuated most of the ultraviolet blackbody radiation from the hot-electron gun used in ion production.

The MCA operated in alternate add and subtract mode that was synchronous with the ion trap's storage and nonstorage cycles. On nonstorage cycles, the trap was emptied after the ion production-excitation phase but before the detection phase by application of a 14-μsec, -75-V pulse to one of the end caps. This sequence allowed background noise not associated with the stored ions to be subtracted while maintaining the symmetry of the creation and detection phases.

The pulsed electron beam's injection energy was varied from 30 eV to 300 eV in preliminary tests and no effect was observed on the radiative-decay rates. At the higher electron energies a time-dependent background, not associated with stored ions, was observed. We chose a relatively low electron-injection energy of 55 eV for production and excitation of C^+ from CO because at this energy no such background was observed. The actual electron-impact energy to create metastable C^+ ions could be much larger than 55 eV, because, after entering the trap through the end cap, the electrons would gain additional energy from the rf field, which has a maximum of 400 V between the ring electrode and the end caps.

Specific ion trap parameters were chosen to optimize the trapping of C^+ and to exclude or to minimize the storage of other ions produced by electron bombardment of the CO source gas. Those ions are CO^+, CO^{2+}, O^+, O^{2+}, and C^{2+}. The storage characteristic, i.e., the stability diagram of this trap, has been mapped by using N^{2+}, N^+, Ar^+, and Ar^{2+} [20]. The stable trajectories of the stored ions can be obtained from the solutions of Mathieu equations. The corresponding Mathieu parameters for trapped C^+ ions were $q_z = 0.57$ and $a_z = -0.086$. At these values both CO^+ and C^{2+} ions were outside the region of stability. Any CO^{2+} would be in quasistable or short-lived states and would dissociate soon after productions [21–23]. Both O^{2+} ($q/m = 8$) and O^+ ($q/m = 16$) ions were expected to be trapped since their Mathieu parameters a_z and q_z were within the stable region of the trap. However, the production of O^{2+} required multiple collisions and the production rate of O^{2+} is four orders of magnitude smaller than that of C^+ ions [24]. Time-of-flight (TOF) spectra were recorded by the TOF mass spectrometer installed behind one of the trap's end caps. Figure 2 shows a time-of-flight mass spectrum of the ions stored in the trap under the storage condition used in our measurements. Only C^+ ions are recorded. The absence of an O^+ signal can be explained by several facts. At the above trap settings for C^+ ion, O^+ ions are not optimally stored because the Mathieu parameters for O^+ are $q_z = 0.43$ and $a_z = -0.065$ [20]. In addition, the O^+ ions are in a nonspherical potential well ($D_r = 16.71$ eV and $D_z = 6.86$ eV). O^+ ions created near the ring electrode may have energy exceeding the well depth along the z direction and may leak out of the trap through the shallower well along the z axial direction. Both O^+ and C^+ ions were produced and detected under the same trap condition when the electron-ejection energy was increased well above 200 eV. In the case where small numbers of O^+ ions were present in the trap, their radiation is not expected to affect our measurement because the decay rates for the parity-forbidden $^4S^\circ$-$^2P^\circ$ transition at 247 nm are more than two orders of magnitude smaller than those measured for the C^+ intersystem transitions [25].

The energy intervals between the $^4P_{5/2}$ and $^4P_{3/2}$, and $^4P_{3/2}$ and $^4P_{1/2}$ levels are 28.3 cm^{-1} and 22.0 cm^{-1} [26],

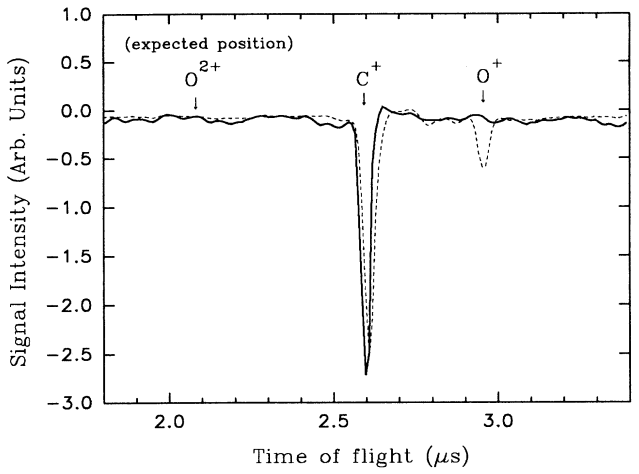

FIG. 2. Time-of-flight mass spectrum for the trapped ions. Under trap conditions: $f = 1.2$ MHz, $V_0 = 400$ V, and $U_0 = 30$ V, C^+ is the only trapped ion detected in the spectrum with the low electron-injection energy of 55 eV. The dashed line represents the ion signal with $U_0 = 20$ V, in which case, O^+ ions are also detected in the trap.

respectively. Thus, collisional processes such as mixing among fine-structure levels and deexcitation (quenching) to the ground term can occur during periods comparable to the radiative lifetime at high source gas density. To minimize these effects we kept the CO pressure at and below 4.4×10^{-8} Torr for the measurements. The lower limit of CO pressure in the measurements was determined by the signal-to-noise ratio. The CO pressure was measured by a Masstorr DX200 residual gas analyzer and a Varian UHV-24 ion gauge.

III. DATA ANALYSIS

The data show (cf. Fig. 3) a multiexponential decay of the photon signal, which is, of course, expected and directly related to the population of the C II metastable levels. We modeled the changes in the ^4P populations by a set of coupled rate equations describing the effects of collisions with the source gas and radiative decay on the populations of the fine-structure levels of the ^4P term. The solution of the differential equations will give us the time dependence of the population density of each fine-structure level. We will use these solutions to determine the radiative-decay rates to the ground term of the fine-structure levels in the ^4P term.

A. Mathematical modeling

The rate equations describing the changes in the populations N_1, N_2, and N_3 of metastable levels $^4P_{1/2}$, $^4P_{3/2}$, and $^4P_{5/2}$, respectively, can be expressed by the following differential matrix equation:

$$\frac{d}{dt}\begin{pmatrix} N_1 \\ N_2 \\ N_3 \end{pmatrix} = \mathbf{R}\begin{pmatrix} N_1 \\ N_2 \\ N_3 \end{pmatrix} , \tag{1a}$$

where $\mathbf{R}$ is a 3×3 matrix with its elements:

$$\begin{aligned} R_{11} &= -A_1 - M(K_1 + K_{12} + K_{13}) , \\ R_{22} &= -A_2 - M(K_2 + K_{21} + K_{23}) , \\ R_{33} &= -A_3 - M(K_3 + K_{31} + K_{32}) , \\ R_{ij} &= MK_{ji} \quad (i,j = 1,2,3 \text{ and } i \neq j) , \end{aligned} \tag{1b}$$

in which $A_1 = A(^4P_{1/2} \rightarrow {}^2P^\circ_{1/2}) + A(^4P_{1/2} \rightarrow {}^2P^\circ_{3/2})$, $A_2 = A(^4P_{3/2} \rightarrow {}^2P^\circ_{1/2}) + A(^4P_{3/2} \rightarrow {}^2P^\circ_{3/2})$, and $A_3 = A(^4P_{5/2} \rightarrow {}^2P^\circ_{3/2})$ are spontaneous decay rates for the $^2P^\circ$-^4P transitions; M is the source gas number density; K_1, K_2, and K_3 are the quenching rate coefficients to the ground term for the three metastable levels; K_{ij} $(i,j = 1,2,3)$ are the collisional mixing rate coefficients from level i to level j among the fine-structure level of the ^4P term, with

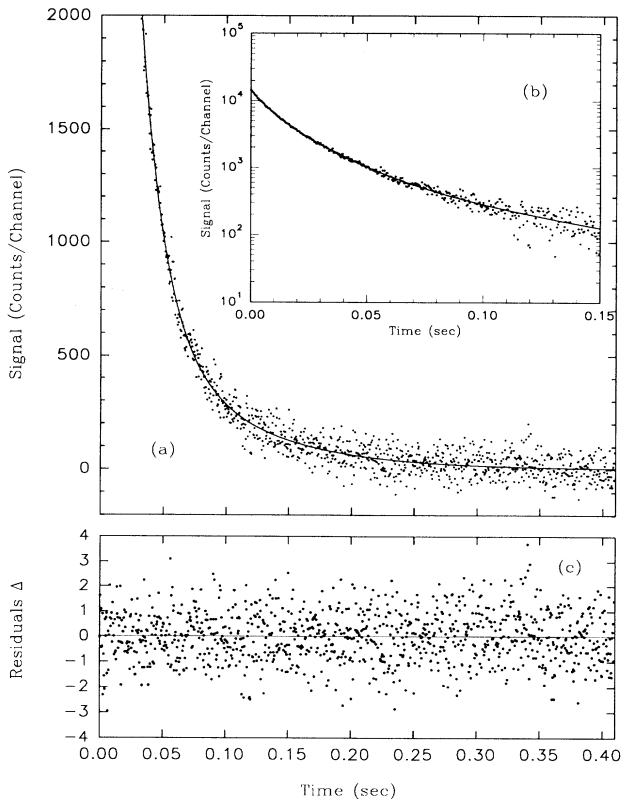

FIG. 3. Decay signals of C II ~233 nm emission as a function of time at 2.2×10^{-8} Torr of CO: (a) linear scale, where only the counts below 2×10^3 per channel are displayed so that the low-count region of the signal can be shown more clearly, and (b) logarithmic scale for the first 0.15 sec of the same data set. The solid curves are the three-exponential fits to the data. The residuals of the fitting are shown in (c).

$$\frac{1}{g_2}K_{12}=\frac{1}{g_1}K_{21}\equiv K_\alpha\ ,$$
$$\frac{1}{g_3}K_{23}=\frac{1}{g_2}K_{32}\equiv K_\beta\ , \tag{2}$$
$$\frac{1}{g_3}K_{13}=\frac{1}{g_1}K_{31}\equiv K_\gamma\ ,$$

where $g_1 = 2$, $g_2 = 4$, and $g_3 = 6$ are the statistical weights of levels $^4P_{1/2}$, $^4P_{3/2}$, and $^4P_{5/2}$, respectively. The first-order linear differential equation (1a) has the general solutions

$$N_1 = a_1e^{-r_1t}+a_2e^{-r_2t}+a_3e^{-r_3}\ ,$$
$$N_2 = b_1e^{-r_1t}+b_2e^{-r_2t}+b_3e^{-r_3t}\ , \tag{3}$$
$$N_3 = c_1e^{-r_1t}+c_2e^{-r_2t}+c_3e^{-r_3t}\ .$$

If the source gas number density M is relatively small, and the condition

$$MK_{ij} \ll |A_k - A_l| \quad (i,j,k,l = 1,2,3 \text{ and } k \neq l)\ , \tag{4}$$

is satisfied, then all the off-diagonal elements of the matrix $\mathbf{R}$ in (1b) may be regarded as small quantities and be treated as perturbations. The first-order solution for Eq. (1a) gives the rates r_1, r_2, and r_3:

$$r_1 = A_1 + M\,(K_1 + g_2K_\alpha + g_3K_\gamma) + \delta_1 + \cdots\ ,$$
$$r_2 = A_2 + M\,(K_2 + g_1K_\alpha + g_3K_\beta) + \delta_2 + \cdots\ , \tag{5a}$$
$$r_3 = A_3 + M\,(K_3 + g_1K_\gamma + g_2K_\beta) + \delta_3 + \cdots\ ,$$

where δ_1, δ_2, and δ_3 are the first-order correction terms, and they are

$$\delta_1 = \frac{g_1g_2(MK_\alpha)^2}{(A_1-A_2)+M\,[K_1-K_2+(g_2-g_1)K_\alpha+g_3(K_\gamma-K_\beta)]} + \frac{g_1g_3(MK_\gamma)^2}{(A_1-A_3)+M\,[K_1-K_3+(g_3-g_1)K_\gamma+g_2(K_\alpha-K_\beta)]}\ ,$$
$$\delta_2 = \frac{g_1g_2(MK_\alpha)^2}{(A_2-A_1)+M\,[K_2-K_1+(g_1-g_2)K_\alpha+g_3(K_\beta-K_\gamma)]} + \frac{g_2g_3(MK_\beta)^2}{(A_2-A_3)+M\,[K_2-K_3+(g_3-g_2)K_\beta+g_1(K_\alpha-K_\gamma)]}\ , \tag{5b}$$
$$\delta_3 = \frac{g_1g_3(MK_\gamma)^2}{(A_3-A_1)+M\,[K_3-K_1+(g_1-g_3)K_\gamma+g_2(K_\beta-K_\alpha)]} + \frac{g_2g_3(MK_\beta)^2}{(A_3-A_2)+M\,[K_3-K_2+(g_2-g_3)K_\beta+g_1(K_\gamma-K_\alpha)]}\ .$$

Although the correction terms δ_1, δ_2, and δ_3 are nonlinear with respect to the number density of the source gas, these terms may be ignored when condition (4) is satisfied.

The first-order solutions for the coefficients of each exponential term in Eqs. (3) are expressed by

$$a_1 \approx N_1(0) - S_{12}N_2(0) - S_{13}N_3(0)\ ,\quad a_2 \approx S_{12}N_2(0)\ ,\quad a_3 \approx S_{13}N_3(0)\ ,$$
$$b_1 \approx S_{21}N_1(0)\ ,\quad b_2 \approx -S_{21}N_1(0) + N_2(0) - S_{23}N_3(0)\ ,\quad b_3 \approx S_{23}N_3(0)\ , \tag{6a}$$
$$c_1 \approx S_{31}N_1(0)\ ,\quad c_2 \approx S_{32}N_2(0)\ ,\quad c_3 \approx -S_{31}N_1(0) - S_{32}N_2(0) + N_3(0)\ ,$$

where

$$\frac{1}{g_1}S_{12} = -\frac{1}{g_2}S_{21} = \frac{MK_\alpha}{(A_1-A_2)+M[K_1-K_2+(g_2-g_1)K_\alpha+g_3(K_\gamma-K_\beta)]}\ ,$$
$$\frac{1}{g_3}S_{32} = -\frac{1}{g_2}S_{23} = \frac{MK_\beta}{(A_3-A_2)+M[K_3-K_2+(g_2-g_3)K_\beta+g_1(K_\gamma-K_\alpha)]}\ , \tag{6b}$$
$$\frac{1}{g_1}S_{13} = -\frac{1}{g_3}S_{31} = \frac{MK_\gamma}{(A_1-A_3)+M[K_1-K_3+(g_3-g_1)K_\gamma+g_2(K_\alpha-K_\beta)]}\ ,$$

and if the conditions of Eq. (4) are satisfied,

$$|S_{ij}| \ll 1 \quad (i,j,k = 1,2,3) , \tag{6c}$$

then in most cases the terms with S_{ij} can be ignored.

The total photon emission rate I for the $^4P \rightarrow {}^2P^\circ$ transition can be expressed by

$$I = A_1N_1 + A_2N_2 + A_3N_3 . \tag{7}$$

By substituting Eqs. (3) and Eqs. (6a) into Eq. (7), the time-dependent photon emission of the C^+ ions has three distinct exponential components:

$$I = I_1e^{-r_1t} + I_2e^{-r_2t} + I_3e^{-r_3t} , \tag{8a}$$

where the intensity components corresponding to the three-exponential decays are

$$\begin{aligned} I_1 &\approx (A_1 + A_2S_{21} + A_3S_{31})N_1(0) \\ &\quad -A_1S_{12}N_2(0) - A_1S_{13}N_3(0) , \\ I_2 &\approx (A_1S_{12} + A_2 + A_3S_{32})N_2(0) \\ &\quad -A_2S_{21}N_1(0) - A_2S_{23}N_3(0) , \\ I_3 &\approx (A_1S_{13} + A_2S_{23} + A_3)N_3(0) \\ &\quad -A_3S_{31}N_1(0) - A_3S_{32}N_2(0) . \end{aligned} \tag{8b}$$

By using Eq. (6c), and the fact that A_2 may be much smaller than A_1 and A_3, the intensity equations of (8b) may further be simplified to

$$\begin{aligned} I_1 &\approx A_1N_1(0) , \\ I_2 &\approx (A_1S_{12} + A_2 + A_3S_{32})N_2(0) , \\ I_3 &\approx A_3N_3(0) . \end{aligned} \tag{8c}$$

Equations (8c) will later be used to verify the level assignment for each decay by comparing them with the measured intensities of each component in the multiexponential decay signals.

B. Data and data analysis

A total of 29 independent measurements were made at the four CO pressures, 1.1, 2.2, 3.3, and 4.4×10^{-8} Torr, with each measurement corresponding to $\sim 1.5 \times 10^5$ cycles of add-subtract sweeps. Each data set y_i ($i = 1$ to 1024) was fitted to a three-exponential decay function consistent with the above model:

$$y(t) = \sum_{j=1}^{3} s_j \exp(-r_jt)$$

using the nonlinear least-squares method with s_j ($j = 1,2,3$) representing the initial intensities, and r_j ($j = 1,2,3$) representing the decay rates of each exponential component. No parameter was used for background since the background subtraction techniques were used in the measurements and the model [Eq. (8a)] does not have a time-independent background. The excellent signal-to-noise ratio of the data and the fact that each of the three-exponential decay rates is different from the other by factors of more than 3 (cf. Sec. IV) greatly improve the reliability of the fit. Figures 3(a) and 3(b) show the sum of the time-dependent signal at 2.2×10^{-8} Torr CO. The result of the three-exponential fit is represented by the solid curve. The residuals, defined by $\Delta_i = [y_i - y(t_i)]/\sigma_i$, are shown in Fig. 3(c), and are evenly distributed about zero. The standard deviation for each data point, σ_i, was used for the weighted fitting, and was determined from the square root of the total number of counts for each channel according to Poisson statistics. Those counts include both photon signal counts, and the background noise counts. The background noise was essentially time independent. The background count per channel was determined from the difference between the total number of signal and noise counts recorded by the digital counter and the total signal counts recorded by MCA divided by the number of channels used in the measurement.

The above data-fitting procedure was performed for each of the 29 data sets and the sum of data for each CO pressure. The reduced χ^2, χ^2_ν ($\chi^2_\nu = \chi^2/\nu$, where ν is the number of degrees of freedom), of all fits for the individual measurements were distributed around 1.00, with 62% of them within the range of ±0.04, 91% within ±0.08, and all within ±0.11, in excellent agreement with the probability distribution function for χ^2_ν [i.e., $P(\chi^2_\nu) = \frac{1}{2^{\nu/2}\Gamma(\nu/2)}\nu(\chi^2_\nu\nu)^{1/2(\nu-2)}\exp(-\chi^2_\nu\nu/2)$, where $\nu = 1018$].

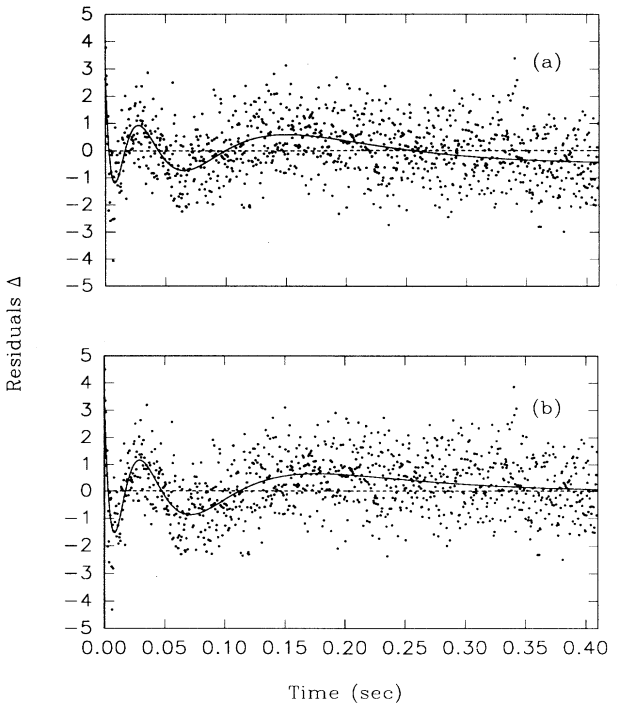

FIG. 4. Residuals of fitting two-exponential decay models to the data. The fitting functions are (a) $y'(t) = \sum_{j=1}^{2} s'_j \exp(-r'_jt) + c$, and (b) $y''(t) = \sum_{j=1}^{2} s''_j \exp(-r''_jt)$. In both cases, the residuals exhibit time-dependent structures. The structures are depicted by the solid curves that are $y(t) - y'(t)$ in (a) and $y(t) - y''(t)$ in (b), where $y(t)$ is the three-exponential decay function (six parameters) fitted to the data.

The excellence of the fits of the data to the three-exponential model was also tested by comparing it with fits to other multiexponential decay functions. First, we used a two-exponential decay plus a background (five parameters) function:

$$y'(t) = \sum_{j=1}^{2} s'_j \exp(-r'_j t) + c \ ,$$

and then a two-exponential decay without a background (four parameters) function:

$$y''(t) = \sum_{j=1}^{2} s''_j \exp(-r''_j t).$$

The residuals of both those fittings exhibited time-dependent structures [see Figs. 4 (a) and 4 (b)], which could be well depicted by the difference of the three-exponential decay function and the two-exponential functions, i.e., $y(t) - y'(t)$ and $y(t) - y''(t)$, respectively. The distribution of the residuals for the three-exponential model is shown in Fig. 5(a) and is consistent with Poisson statistics where the theoretical distribution curve

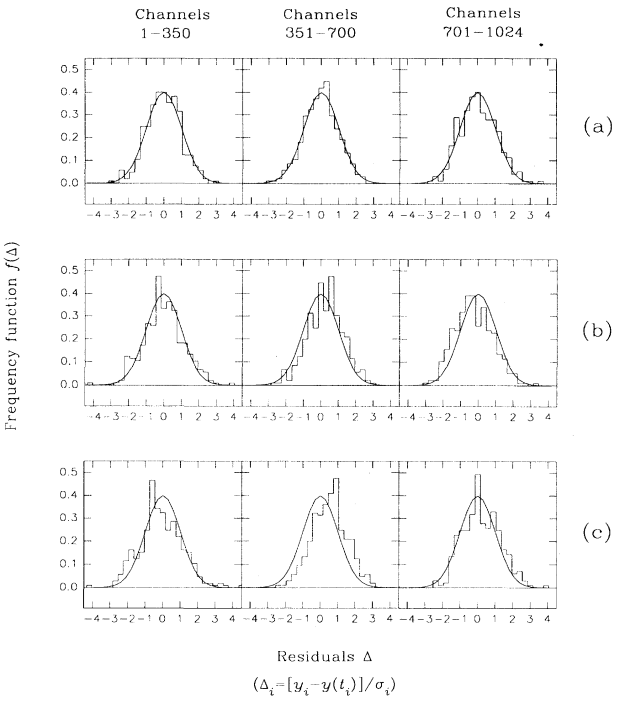

FIG. 5. Comparison of the Poisson distribution functions of residuals with the residuals distributions as results of using different models fitted to the data. The comparison is made for each of three different periods of the decay. The functions used in the fits are: (a) three-exponential without background; (b) two-exponential plus a background; and (c) two-exponential without background. The histograms are frequency distributions of the residuals. The smooth curves are frequency functions of the residuals according to the Poisson statistics, which are Gaussian: $P(\Delta) = 1/\sqrt{2\pi}\exp(-\Delta^2/2)$, since the signal counts per channel exceeds a few hundred.

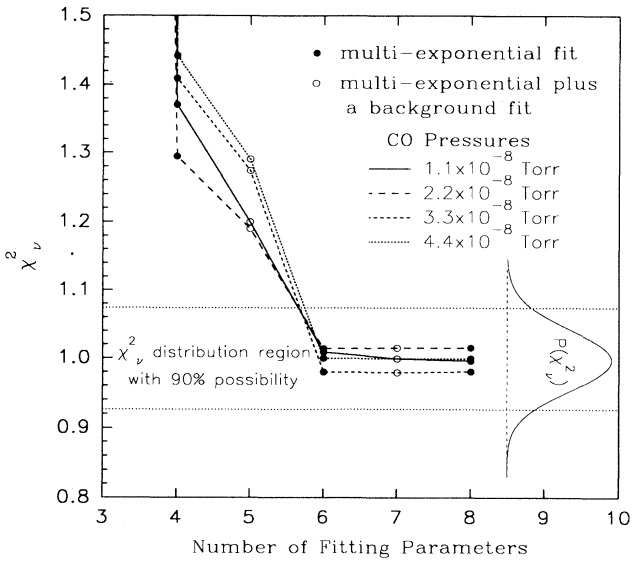

FIG. 6. χ^2_ν values of the fits to different multiexponential models. The three-exponential fit (six parameters) gives χ^2_ν values about 1.00 and satisfies the theoretical prediction. The χ^2_ν of the less-than-six-parameter fits (two- or one-exponential) are beyond the possible distribution region represented by $P(\chi^2_\nu)$. The models with extra parameters, other than the six needed for our three-exponential model, give no improvement of χ^2_ν. The χ^2_ν of the three-parameter fit are about 6–10. The lines joining the χ^2_ν values are visual aids and only indicate equal CO pressure.

is Gaussian: $P(\Delta) = (1/\sqrt{2\pi})\exp(-\Delta^2/2)$, at signal counts per channel exceeding a few hundred. The deviation of the residuals distribution from Poisson statistics for other multiexponential models is clearly revealed in Figs. 5(b) and 5(c). The χ^2_ν of these fittings were as high as 1.2 to 1.3 for five-parameter fits and 1.3 to 1.4 for four-parameter fits. These χ^2_ν values are outside the possible χ^2_ν distribution region (cf. Fig. 6). If we used more than a six-parameter function, e.g., a three-exponential decay plus a background function or a four-exponential decay function without a background, to fit our data, the χ^2_ν did not improve (see Fig. 6). In addition, no significant changes of the three decay rates were observed by introducing the extra parameters. The function with least parameters is the three-exponential one and this is consistent with the model proposed in Eq. (7). We conclude that the six-parameter three-exponential decay function adequately describes the radiative processes of C^+ in the low-pressure environment chosen for the measurement.

The three decay rates for each CO pressure used could be obtained by a weighted average of the decay rates determined from each individual measurement at that pressure or equally well obtained from the sum of the signal at that pressure. The results obtained were essentially the same. The statistical errors shown were estimated from the fluctuations of the results from the separate measurements, which were also in agreement with those calculated with the nonlinear least-squares fitting algo-

rithm of the summed data. Plots of the decay rates determined for each transition versus CO pressure are shown in Fig. 7. The radiative-decay rates were evaluated by extrapolating the rates to zero CO pressure according to Eq. (5a). At the low CO pressure range chosen in our measurement, the first-order correction terms δ_j can be neglected and a linear fit used to determine the A_j values. In accordance with Eq. (5a) the combined collisional mixing rates and the quenching rates by CO gas can be estimated from the slopes of the radiative-decay rate versus CO pressure curves (Fig. 7).

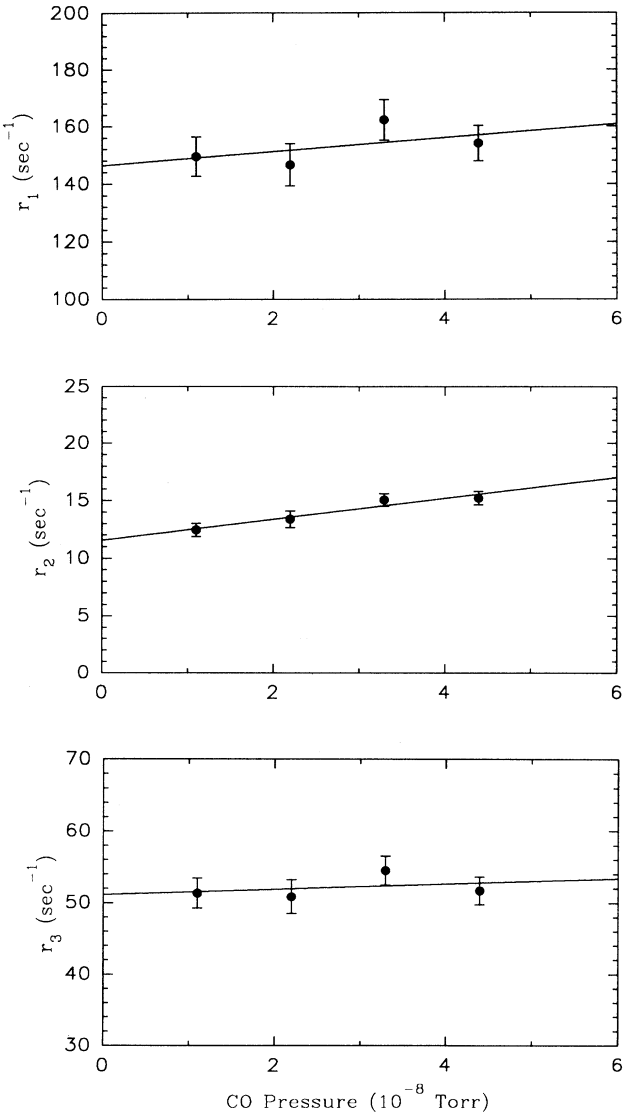

FIG. 7. Plots of the decay rates as functions of CO pressure. The decay rates r_1, r_2, and r_3 are assigned to decays of the levels $^4P_{1/2}$, $^4P_{3/2}$, and $^4P_{5/2}$, to the ground term $2s^22p(^2P^\circ)$, respectively. The intercepts at zero pressure give the radiative-decay rates for corresponding transitions. The uncertainties represented by error bars are statistical standard deviations.

TABLE I. Comparison of the ratios of the measured initial intensities of the three-exponential components with those derived by Eq. (8c).

CO pressure (10^{-8} Torr)	$I_1 : I_2 : I_3$ Measured	$I_1 : I_2 : I_3$ Derived by Eq. (8c)[a]
1.1	0.92(0.07) : 0.13(0.02) : 1	0.92 : 0.15 : 1
2.2	0.94(0.08) : 0.13(0.01) : 1	0.92 : 0.15 : 1
3.3	0.90(0.06) : 0.15(0.02) : 1	0.92 : 0.15 : 1
4.4	1.06(0.07) : 0.14(0.02) : 1	0.92 : 0.15 : 1

[a]Approximately the same at each CO pressure.

IV. RESULTS AND DISCUSSION

The radiative-decay rates were obtained by extrapolating the rates to their values at the zero CO pressure. The values obtained are 146.4(8.3) s^{-1}, 11.6(0.8) s^{-1}, and 51.2(2.6) s^{-1} for the transitions from the fine-structure levels $^4P_{1/2}$, $^4P_{3/2}$, and $^4P_{5/2}$ to the ground term, respectively. The quoted uncertainties are statistical standard deviations.

The assignment of those rates to the corresponding transitions was guided by comparing the measured values with theoretical predictions. However, in addition, we compared the measured initial intensity ratios of the three decay components, $s_1 : s_2 : s_3$, with the calculated results, $I_1 : I_2 : I_3$, where I_1, I_2, and I_3 are expressed in Eq. (8c). Here the values of A_j were substituted by our measured values of the radiative-decay rates, and $N_1(0)$, $N_2(0)$, and $N_3(0)$ were determined with the assumption that the three metastable levels were populated during electron-impact excitation in accordance with their statistical weights g_1, g_2, and g_3. We also included a small correction term to account for the depopulations of these levels during the 0.5-msec relaxation period. We also ignored the S_{12} and S_{32} terms in Eq. (8c) because these terms are dependent on mixing and quenching cross section and CO density. However, by assuming a relatively larger cross section of 10^{-14} cm^2, these two terms are negligibly small at the CO pressure range chosen for the measurement. The comparison of the intensity ratios is shown in Table I and the agreement supports the level assignment without ambiguity.

We determined the combined collisional rate coefficient of the $^4P_{3/2}$ level with CO, $K_2 + K_{21} + K_{23}$, from the slope of r_2 as a function of the CO pressure, and the combined rate is $2.8(0.7)\times10^{-9}$ $cm^3\,s^{-1}$.

The residual gas in our high-vacuum system consisted of water and nitrogen in the 10^{-10} Torr range. However, residual hydrogen gas was about 1×10^{-8} Torr. This small amount of hydrogen can cause an overestimate of the decay rates by about 0.9 s^{-1} if we assume that the combined rate coefficient for $^4P_{3/2}$ in collision with CO is comparable to the combined rate coefficients of those levels in collision with molecular hydrogen. However, we believe hydrogen has a smaller collisional cross section than CO, because CO has a permanent electric-dipole

TABLE II. Measured and calculated radiative transition probabilities for the $^2P^\circ$-^4P intersystem lines of C II.

	A ($\sec^{-1}$)				
Transition	This work 1993	LDHK[c] 1985	SLBJCWC[d] 1981	NS[e] 1981	DT[f] 1978
$^4P_{1/2} \rightarrow {}^2P^\circ_{1/2}$	–	74.4	56.4	55.3	42.5
$^4P_{1/2} \rightarrow {}^2P^\circ_{3/2}$	–	77.8	65.7	65.5	40.2
Σ[a]	146.4(+8.3,−9.2)	152.2	122.1	120.8	82.7
$^4P_{3/2} \rightarrow {}^2P^\circ_{1/2}$	–	1.70	2.8	1.71	1.01
$^4P_{3/2} \rightarrow {}^2P^\circ_{3/2}$	–	12.4	8.5	5.24	8.11
Σ[b]	11.6(+0.8,−1.7)	14.1	11.3	6.95	9.12
$^4P_{5/2} \rightarrow {}^2P^\circ_{3/2}$	51.2(+2.6,−3.5)	53.9	37.6	43.2	34.4

[a]Σ: $^4P_{1/2} \rightarrow {}^2P^\circ_{1/2,3/2}$.

[b]Σ: $^4P_{3/2} \rightarrow {}^2P^\circ_{1/2,3/2}$.

[c]Calculated by Lennon *et al.* [12].

[d]Empirical values derived from Nussbaumer and Storey [15] by Stencel *et al.* [10].

[e]Calculated by Nussbaumer and Storey [15].

[f]Calculated by Dankwort and Trefftz [13].

moment. The final results, including systematic uncertainties and theoretical calculations, are shown in Table II.

The measured values of A_1 and A_3 have uncertainties of (+5.7,−6.3%) and (+5.1,−6.8%), respectively. Our values are in good agreement with the values calculated by Lennon *et al.* [12], but are about 20% larger than the values of Nussbaumer and Storey [15] and of Stencel *et al.* [10]. The uncertainty for the measured A_2 value is (+7,−15%). This value is 18% smaller than that calculated by Lennon *et al.* [12] and about 67% larger than that of Nussbaumer and Storey [15], and in agreement with that of Stencel *et al.* [10].

ACKNOWLEDGMENTS

We acknowledge the technical assistance of Heinz Knocke and Milton Lewis. A discussion with David P. Shelton on the data fitting is appreciated. V.H.S.K. acknowledges the discussion with Anthony G. Calamai on the data analysis using multiexponential fit on analogous radiative decays in Si II. This work is supported in part by Grant Nos. RII-8410674 from the National Science Foundation (EPSCoR) to the University of Nevada system and by the State of Nevada. W.H.P. acknowledges the support from the NASA Grant Nos. NAGW-1687 and 1596 to Harvard University.

[1] P. G. Judge, Mon. Not. R. Astron. Soc. **221**, 119 (1986); **223**, 239 (1986).

[2] Kenneth G. Carpenter, Richard D. Robinson, Glen M. Wahlgren, Thomas B. Ake, Denni C. Ebbets, Jeffrey L. Linsky, Alexander Brown, and Frederick M. Walter, Astrophys. J. Lett. **377**, L45 (1991).

[3] J. L. Linsky, A. Brown, and K. G. Carpenter, *The First Year of HST Observations*, edited by A. L. Kinney and J. C. Blades (Space Telescope Science Institute, Baltimore, MD, 1991).

[4] G. A. Doschek, U. Feldman, and L. Cohen, Astrophys. J. Suppl. **33**, 101 (1977).

[5] G. A. Doschek, U. Feldman, M. E. Van Hoosier, and J.-D. F. Bartoe, Astrophys. J. Suppl. **31**, 417 (1976).

[6] P. Brekke, O. Kjeldsech-Moe, J. -D. F. Bartoe, and G. E. Brueckner, Astrophys. J. Suppl. **75**, 1337 (1991).

[7] H. Nussbaumer and H. Schild, Astron. Astrophys. **101**, 118 (1981).

[8] M. A. Hayes and H. Nussbaumer, Astron. Astrophys. **161**, 287 (1986).

[9] U. Feldman and G. A. Doschek, Astron. Astrophys. **79**, 357 (1979).

[10] R. E. Stencel, J. L. Linsky, A. Brown, C. Jordan, K. G. Carpenter, R. F. Wing, and S. Czyzak, Mon. Not. R. Astron. Soc. **196**, 47 (1981).

[11] G. A. Doschek, *Autoionization*, edited by A. Temkin (Plenum, New York, 1985), p. 171.

[12] D. J. Lennon, P. L. Dufton, A. Hibbert, and A. E. Kingston, Astrophys. J. **294**, 200 (1985).

[13] W. Dankwort and E. Trefftz, Astron. Astrophys. **65**, 93 (1978).

[14] H. Nussbaumer and P. J. Storey, Astron. Astrophys. **71**, L5 (1979).

[15] H. Nussbaumer and P. J. Storey, Astron. Astrophys. **96**, 91 (1981).

[16] B. Edlén, Phys. Scr. **23**, 1079 (1981).

[17] A. G. Calamai, P. L. Smith, V. H. S. Kwong, and W. H. Parkinson, in *Proceedings of the 4th International Colloquium on Atomic Spectra and Oscillator Strengths for Astrophysical and Laboratory Plasmas*, National Institute of Standards and Technology Publication No. SP-850, edited by J. Sugar and D. S. Leckrone (National Insti-

tute of Standards and Technology, Washington, DC, in press).
[18] Victor H. S. Kwong, Z. Fang, T. T. Gibbons, W. H. Parkinson, and Peter L. Smith, Astrophys. J. (to be published).
[19] H. G. Dehmelt, Adv. At. Mol. Phys. **3**, 53 (1967).
[20] V. H. S. Kwong, T. T. Gibbons, Z. Fang, J. Jiang, H. Knocke, Y. Jiang, B. Ruger, S. Huang, E. Braganza, W. Clark, and L. D. Gardner, Rev. Sci. Instrum. **61**, 1931 (1990).
[21] G. Dujardin, L. Hellner, M. Hamdan, A. G. Brenton, B. J. Olsson, and M. J. Besnard-Ramage, J. Phys. B **23**, 1165 (1990).
[22] S. Mazumdar, F. A. Rajgara, V. R. Marathe, C. Badrinathan, and D. Mathur, J. Phys. B **21**, 2815 (1988).
[23] J. M. Curtis and R. K. Boyd, J. Chem. Phys. **80**, 1150 (1984).
[24] J. F. O'Halon, *A User's Guide to Vacuum Technology*, 2nd ed. (Wiley, New York, 1989).
[25] M. J. Seaton and D. E. Osterbrock, Astrophys. J. **125**, 66 (1957).
[26] S. Bashkin and J. O. Stoner, *Atomic Energy Levels and Grotrian Diagrams* (Elsevier, New York, 1975), Vol. 1, p. 77.